

Experimental and theoretical investigation of $4f^3 \leftrightarrow 4f^2 5d$ interconfigurational transitions in $\text{Nd}^{3+}:\text{LiYF}_4$ crystals

A. Collombet,¹ Y. Guyot,¹ M. F. Joubert,¹ M. Laroche,² J. Margerie,² R. Moncorgé,^{2,*} and E. Descroix³¹Laboratoire de Physico-Chimie des Matériaux Luminescents, UMR 5620 CNRS, Université Lyon 1, F-69622 Villeurbanne Cedex, France²Centre Interdisciplinaire de Recherches Ions et Lasers, UMR 6637 CEA-CNRS-ISMRA,

Université de Caen, F-14050 Caen Cedex, France

³Laboratoire du Traitement du Signal et de l'Information, UMR 5516 CNRS, Université Jean Monnet,

F-42023 Saint-Etienne Cedex, France

(Received 18 July 2002; revised manuscript received 15 April 2003; published 30 July 2003)

A complete spectroscopic investigation of the $4f^3 \leftrightarrow 4f^2 5d$ optical transitions of the Nd^{3+} ion is performed in the case of $\text{Nd}:\text{LiYF}_4$, based on emission, excitation, ground-state absorption as well as excited-state absorption measurements. The global shape of all the experimental spectra is well reproduced by means of crystal-field calculations of the $4f^2 5d$ sublevels, and the differences observed between polarized spectra on one hand, and between those recorded at low and room temperatures on the other hand, are successfully accounted for. It is also found that the absorption barycentre is shifted toward higher $4f^2 5d$ energies when the chosen initial $4f^3$ sublevel itself is shifted toward higher energies. This behavior is assigned to a total or partial “memory” during the optical transition for the expectation values of different terms of the hamiltonian, especially the electrostatic ones. It is demonstrated that this effect should not be specific of $\text{Nd}^{3+}:\text{LiYF}_4$ and that it should occur, on the contrary, in every crystalline matrix and for any rare-earth ion from Pr^{3+} ($4f^2$) to Tm^{3+} ($4f^{12}$).

DOI: 10.1103/PhysRevB.68.035115

PACS number(s): 78.20.Bh, 78.40.Ha, 78.55.Hx, 71.70.Ch

I. INTRODUCTION

The development of convenient and efficient laser sources covering a large spectral range in the UV or VUV could meet the requirements of numerous applications in biology, medicine, microelectronics, environmental sciences, etc. There is, in particular, an increasing interest in the study of $4f^{n-1} 5d \leftrightarrow 4f^n$ interconfigurational transitions within rare-earth ions embedded into wide band-gap crystals. The broad-band emission resulting from $4f^{n-1} 5d \rightarrow 4f^n$ transitions may provide the possibility of generating efficient and tunable UV or VUV laser radiations, and the development of solid-state lasers based on such transitions is very attractive because of the relative simplicity and the practical advantages such laser sources could present over the already existing ones.

Among the trivalent rare-earth ions studied for this purpose, Nd^{3+} is a particularly promising candidate because laser action has already been demonstrated with $\text{Nd}^{3+}:\text{LaF}_3$ and $\text{Nd}^{3+}:\text{LiYF}_4$ single crystals at 172 nm and 260 nm, respectively, after direct excitation into the $4f^2 5d$ absorption band by pulsed sources at 146 or 157 nm.^{1–3} Furthermore, the energy-level scheme of the $4f^3$ configuration of the Nd^{3+} ion presents three metastable states, $^4F_{3/2}$, $^2P_{3/2}$, and $^4D_{3/2}$, that can be used as intermediate states for a multistep excitation. Such an excitation process, involving less energetic photons, should reduce the generation of absorbing color centres which usually form under high-energy VUV excitation.

In the present paper, we chiefly focus on the study of $\text{Nd}^{3+}:\text{LiYF}_4$. The location of the bottom of the $4f^2 5d$ band of Nd^{3+} in this crystal is compatible with an excitation with UV photons from one of the three metastable levels mentioned above. Among them, $^4F_{3/2}$ and $^4D_{3/2}$ are interesting

because they can be easily and efficiently populated with convenient laser sources such as an IR laser diode at 800 nm for the first one and a frequency-tripled $\text{Nd}:\text{YAG}$ laser at 355 nm for the latter. Pumping of the $^4D_{3/2}$ level could be more advantageous because the successive absorption of two 355-nm photons directly populates the $4f^2 5d$ configuration, as is proved by the presence of the corresponding anti-Stokes fluorescence, and the process would thus require only one pump-laser device. Unfortunately, preliminary excited-state excitation (ESE) measurements indicate that the second step $^4D_{3/2} \rightarrow 4f^2 5d$ around 355 nm is rather weak, so that this excitation mechanism is not efficient enough for generating coherent VUV radiation with only one pump laser, while the mechanisms using two lasers (either via $^4D_{3/2}$ or via $^4F_{3/2}$) remain promising.⁴

Before making any attempt to obtain laser action with $\text{Nd}^{3+}:\text{LiYF}_4$ by using such a two-step excitation, it is necessary to perform a careful spectroscopic investigation of the $4f^3 \leftrightarrow 4f^2 5d$ transitions. Indeed, contrary to the extensively studied $4f^3 \leftrightarrow 4f^3$ transitions, only few papers report on experimental $4f^3 \leftrightarrow 4f^2 5d$ spectra,^{5–8} and the efforts to reproduce these spectra by calculations are quite rare. To our knowledge, only two recent papers report on modeling of these transitions for Nd^{3+} .^{9,10} So as to enlarge our knowledge of these transitions, we undertook the measurement of polarized emission and excited-state absorption (ESA) spectra at room and low temperatures. The results obtained are reported here and compared with the numerical predictions obtained from a calculation of the $4f^2 5d$ sublevels and of the $4f^3 \rightarrow 4f^2 5d$ electric dipolar transitions (Secs. II, III, and IV below). In particular, we observe experimentally that ESA from the $^4D_{3/2}$ level in the 230–330 nm wavelength domain corresponding to the bottom of the $4f^2 5d$ configuration, al-

though stronger than initially reported,⁴ is still significantly weaker than ESA from the ${}^4F_{3/2}$ level which itself is noticeably smaller than ${}^4I_{9/2}$ ground-state absorption (GSA), both toward the same $4f^25d$ sublevels. In fact, calculation shows that the total absorption from ${}^4I_{9/2}$, ${}^4F_{3/2}$, and ${}^4D_{3/2}$ toward $4f^25d$ states have similar integrated intensities, but that the absorption barycentre is shifted to higher $4f^25d$ energies when the initial $4f^3$ level itself is shifted to higher energies. This phenomenon is studied in detail in Sec. V and is shown in Sec. VI to be quite general; the same behavior is expected for every ion from Pr^{3+} to Tm^{3+} in any crystalline surrounding.

II. EXPERIMENTAL CONDITIONS

LiYF_4 crystallizes in the tetragonal structure of the scheelite (space group C_{4h}^6) and Nd^{3+} substitutes for Y^{3+} ions at sites of S_4 symmetry. An orientated LiYF_4 single crystal doped with 1.4 at. % neodymium was used for the measurements.

Emission spectra were recorded using two-step excitation with the aid of the 355-nm radiation (12 ns pulse length and 10 Hz repetition rate) of a frequency-tripled Nd:YAG laser (QUANTEL). Such an excitation mechanism is not very efficient, as pointed above, but it is sufficient to observe $4f^25d$ fluorescence. The spectra were analyzed with a 1-m monochromator (Hilger&Watts, Monospek 1000), using a UV (150–450 nm) grating with 1200 grooves/mm. The luminescence signal was detected by a photomultiplier (EMI 9789Q) and fed into a boxcar (Stanford 250) and a numerical oscilloscope (Lecroy 9400).

ESA from the ${}^4F_{3/2}$ metastable state was measured by a standard pump-probe technique consisting of a pulsed dye laser and a cw deuterium lamp (185–300 nm). The dye laser was used to populate the ${}^4F_{3/2}$ metastable (via direct excitation of the ${}^4G_{5/2}$ or ${}^4G_{7/2}$ levels, followed by rapid multiphonon relaxation down to ${}^4F_{3/2}$), and the intensity of the probe light provided by the deuterium lamp and transmitted through the crystal was measured in the presence or absence of the pump beam via a Jobin-Yvon H20 monochromator, followed by an EMI 9789Q photomultiplier.

Emission and ${}^4F_{3/2}$ ESA spectra were recorded in π (electric field parallel to the c axis) and σ (electric field perpendicular to the c axis) polarizations. These polarizations were separated by an MgF_2 Rochon prism, permitting the registration of polarized spectra in the whole UV spectral domain, up to the limit set by air absorption.

ESA from ${}^4D_{3/2}$ was measured between 230 and 350 nm by using a pump-probe setup based on two synchronized Nd:YAG pulsed lasers (7 ns pulse length and 10 Hz repetition rate). The pump beam used to populate ${}^4D_{3/2}$ was the frequency-tripled radiation at 355 nm of one of them (QUANTEL) and the probe beam the radiation produced by the second (BMI) in association with various wavelength converters (nonlinear crystals, OPO, and dye lasers) depending on the investigated wavelength domain. This technique was preferred to the previous one because of the short emission lifetime (1 μs) of the ${}^4D_{3/2}$ level. The delay between the two lasers was adjusted to a few tens of ns. The sample was

sandwiched between two 0.5 mm diameter pinholes and absorbed 38% of the 2.1 mJ incident pump energy at 355 nm. The experiment consisted in comparison of the probe light intensity transmitted by the sample when the pump beam was on or off, this intensity being normalized to the number of incident probe photons. Two pyroelectric detectors were used for these measurements and the simultaneous acquisition of the two signals was performed with a numerical oscilloscope (DSA-TEKTRONIX).

Low-temperature (12 K) spectra were performed by mounting the sample on the cold finger of a closed circuit helium refrigeration system (SMC-TBT-Air Liquid) and the monochromator slits were reduced as much as possible in order to get the best spectral resolution and be able to observe zero-phonon lines.

For a more complete comparison with numerical predictions, we also recorded ${}^4I_{9/2} \rightarrow 4f^25d$ VUV ground-state absorption (GSA)—using a McPherson 302 double beam spectrophotometer—and ground-state excitation (GSE) as well as ${}^4D_{3/2} \rightarrow 4f^25d$ ESE spectra by selecting the $4f^25d \rightarrow 4f^3$ emission with a solar blind filter (225–325 nm). The experimental setups used to record the GSE and ESE spectra have been described elsewhere.⁴

III. CALCULATION HYPOTHESES AND METHODS

Numerical predictions of the $4f^2 \rightarrow 4f5d$ optical transitions of Pr^{3+} in LiYF_4 have been previously carried out.¹¹ We extended this study to the case of Nd^{3+} . The S_4 axis of the Nd^{3+} site is taken as Oz. We use basis sets of pure LS coupling wave functions $|f^3\alpha SLJM\rangle$ and $|(f^2S_1L_1, d)SLJM\rangle$. For f^3 configuration, α is a supplementary quantum number distinguishing terms with the same S and L values. The Hamiltonian is

$$H = H_{ee} + V_{SO} + V_{crys}, \quad (1)$$

where H_{ee} is the electrostatic interaction between optical electrons, V_{SO} is the spin-orbit coupling, and V_{crys} is the coupling of the optical electrons with the crystal field. H is diagonalized separately in the $4f^3$ and in the $4f^25d$ configurations using the parameters of Table I.

The normalized eigenfunctions resulting from H diagonalization are called $|\Psi_i\rangle$'s and $|\Phi_i\rangle$'s for the $4f^3$ and $4f^25d$ configurations, respectively. i is an index which labels the levels in order of increasing energies within each configuration. Because of Kramers theorem, each sublevel is doubly degenerate, so that there are only 182 sublevels for $4f^3$ and 455 for $4f^25d$. Moreover, these sublevels fall into two groups corresponding to irreducible representations $\Gamma_{5,6}$ or $\Gamma_{7,8}$ of the S_4 point group.

The integrated absorption cross section from sublevel $|\Psi_{i'}\rangle$ to sublevel $|\Phi_i\rangle$ with light polarization p ($p=0, +, \text{ or } -$ for $\pi, \sigma^+, \text{ or } \sigma^-$ polarized light, respectively) is given by

$$I_{i'i}^p \equiv \int \sigma_{i'i}^p(\nu') d\nu' = \frac{2\pi^2}{h\epsilon_0 c} \nu_{i'i} \frac{(n^2+2)^2}{9n} |\langle \Phi_i | D_p | \Psi_{i'} \rangle|^2, \quad (2)$$

TABLE I. Parameters for calculations (in cm^{-1}).

$F^{(2)}(\text{ff})$	73519 ^a	$\zeta(f)$	885 ^a
$F^{(4)}(\text{ff})$	53143 ^a	$\zeta(d)$	1077 ^b
$F^{(6)}(\text{ff})$	34924 ^a	$B_{20}(f)$	532 ^c
$F^{(2)}(\text{fd})$	21221 ^b	$B_{40}(f)$	-934 ^c
$F^{(4)}(\text{fd})$	15927 ^b	$B_{44}(f)$	1186 ^c
$G^{(1)}(\text{fd})$	9922 ^b	$B_{60}(f)$	-76 ^c
$G^{(3)}(\text{fd})$	11587 ^b	$B_{64}(f)$	1006-334i ^c
$G^{(5)}(\text{fd})$	8300 ^b	$B_{20}(d)$	7082 ^d
$\alpha(\text{ff})$	20 ^a	$B_{40}(d)$	-13314 ^d
$\beta(\text{ff})$	-592 ^a	$B_{44}(d)$	15855 ^d
$\gamma(\text{ff})$	1507 ^a		

^aFrom Ref. 12.

^bLinearly interpolated between the Pr^{3+} and Lu^{3+} free ion values of Refs. 13 and 14, with an empirical multiplicative factor 0.962 (electrostatic parameters) or 0.987 (ζ) to take into account the reduction of electrostatic and spin-orbit couplings within the crystal.¹¹

^cFrom Ref. 12, after a rotation around the S_4 -axis to cancel the imaginary part of B_{44} .

^dValues for Pr^{3+} (Ref. 11) multiplied by $\rho_k(\text{Nd})/\rho_k(\text{Pr})$, from Table II of Ref. 15. The spectral distance d'_0 between the lowest sublevels of $4f^25d$ and $4f^3$ configurations has been adjusted as 56 760 and 55 780 cm^{-1} for absorption and emission spectra, respectively. The radial monoelectronic integral $\langle r \rangle_{fd} = \langle \mathcal{R}_{5d} | r | \mathcal{R}_{4f} \rangle$ is 0.245 Å, from Ref. 11.

where $\nu_{i'i}$ is the central wave number of the line, $\sigma_{i'i}^p$ its cross-section in p polarization, n is the crystalline matrix refractive index, and D_p is the p component of the electric dipole operator \vec{D} . Matrix elements $\langle \Phi_i | D_p | \Psi_{i'} \rangle$ are readily calculated from the eigenfunctions obtained through diagonalization of H .

The spectral breadths of individual $4f^3 \rightarrow 4f^25d$ components are noticeably greater than those of intraconfigurational $4f^3 \rightarrow 4f^3$ lines. Moreover, a great number of $4f^25d$ sublevels are involved, so that few individual components are resolved at low temperature and none at all at room temperature (see Sec. IV). Therefore, we make simulations of GSA and ESA spectra by assuming a Gaussian shape, with equal breadth δ for all individual components of the spectrum. We calculate

$$\sigma^p(\nu) = \sum_{i,i'} \bar{\omega}_{i'} I_{i'}^p \frac{\exp\left[-\left(\frac{\nu - \nu_{i'i}}{\delta'}\right)^2\right]}{\sqrt{\pi} \delta'}, \quad (3)$$

where $\delta' = \delta/[2\sqrt{\ln(2)}]$. The i summation is over all 455 sublevels of the $4f^25d$ configuration, whereas the i' summation is limited to the few consecutive initial $4f^3$ sublevels that are thermally populated (with Boltzmann equilibrium relative populations $\bar{\omega}_{i'}$) in the experiment, to be simulated. The full width at half maximum δ of individual components is taken as 1600 cm^{-1} at 295 K (like in Ref. 11) and 750 cm^{-1} at 12 K (adjustment for best fit of calculated and observed spectra). For computing stimulated emission or

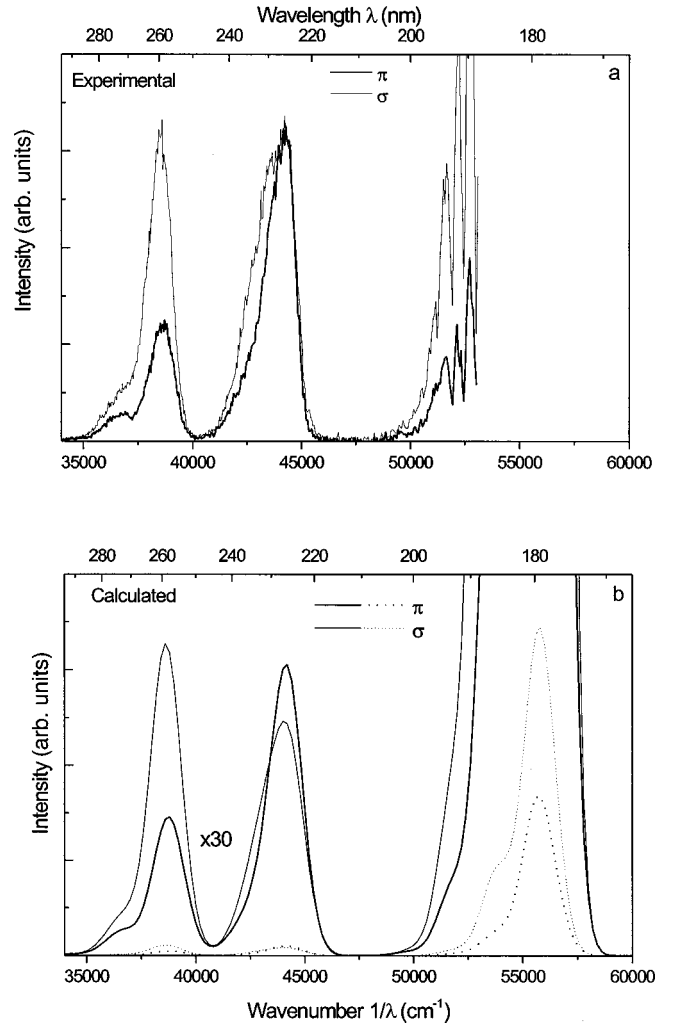


FIG. 1. Room-temperature (a) experimental and (b) simulated polarized spontaneous emission spectra. The full lines in Fig. 1(b) correspond to a $30 \times$ zoom.

spontaneous emission spectra, we use straightforward modifications of formulas (2) and (3).

IV. EXPERIMENTAL RESULTS AND DISCUSSION

A. Emission

The unpolarized UV fluorescence spectrum of Nd^{3+} in LiYF_4 at room temperature has been reported several times in the literature.⁵⁻⁸ The spectral domain of emission, corresponding to $4f^25d \rightarrow 4f^3$, spreads from 170 nm to 280 nm and the spectrum shows three strong and broad bands peaking around 179 nm, 227 nm, and 259 nm with a clear shoulder around 275 nm. Our polarized emission spectra are presented in Fig. 1(a). Because the experiments were not performed under vacuum, photons with a wavelength less than 190 nm were strongly absorbed by air. However, it is known experimentally that the $4f^25d \rightarrow 4I_1$ VUV emission band centered around 179 nm is about ten times more intense than those at 227 or 259 nm⁸ and our calculated spectra presented in Fig. 1(b) show that the multiplicative factor should be of the order of 30 for the 259-nm band in σ po-

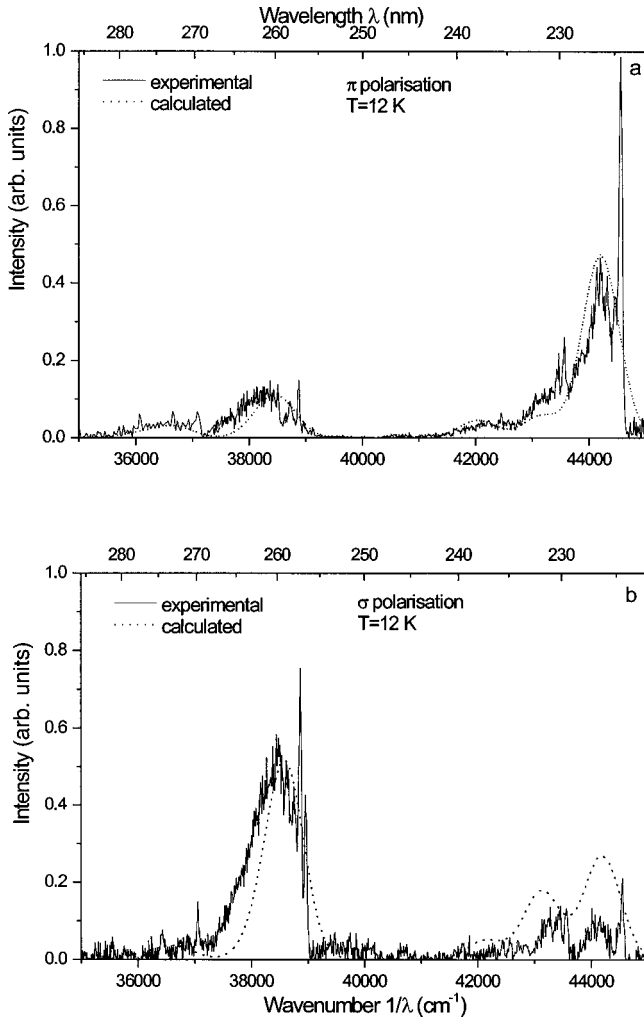


FIG. 2. Low-temperature experimental and simulated spontaneous emission spectra (a) in π and (b) in σ polarization. The same normalization factor is taken for both polarizations.

larization. So, it is very likely that the most favourable emission for laser operation will be this VUV emission band.

Because our spectra could not be recorded over the entire emission domain, they did not allow calculation of the stimulated emission cross sections. An estimate can be made, however, by using the data of Ref. 8 and the Fuchtbauer-Ladenburg method. Thus, stimulated emission cross sections of 4.7×10^{-18} and 2.1×10^{-18} cm^2 for the bands at 179 ($55\,800\text{ cm}^{-1}$) and 259 nm ($38\,600\text{ cm}^{-1}$), respectively, are found. This can be compared with the results of our theoretical treatment which yields, for example, in σ polarization and at room temperature, stimulated emission cross sections of 5.6×10^{-18} and 1.1×10^{-18} cm^2 at 179 and 259 nm, respectively. We also compute a room temperature $4f^25d$ radiative lifetime of 16.5 ns, in perfect agreement with the value of 16.7 ns we measured under excitation with a pulsed hydrogen lamp.

At low temperature ($\approx 12\text{ K}$) (see in Fig. 2), the structures of the emission bands become more pronounced because of reduction of vibronic effects. Thus, the previous broad bands are now decomposed into three or two narrower ones lying,

respectively, at 226, 230, and 237 nm and at 260 and 274 nm. They are more strongly polarized than at room temperature, which suggests that several thermally populated $4f^25d$ states with different symmetries are involved at room temperature in the electric dipole transitions. Zero-phonon lines also clearly appear below about 150 K (see in Fig. 2) and the energy spacings between these zero-phonon lines are confronted with the energy differences between the well known $4f^3$ energy levels of $\text{Nd}:\text{LiYF}_4$.¹² In this way, the various zero-phonon lines can be assigned to transitions from a $4f^25d$ initial state located at $56\,160 \pm 50\text{ cm}^{-1}$ to various Stark components of several $4f^3$ levels (see in Table II). Each zero-phonon line is associated with a broader vibronic sideband and the spectral distance between the position of the zero-phonon line and the maximum of the broadband is nearly constant: $380 \pm 30\text{ cm}^{-1}$. This is the reason why parameter d'_0 introduced in Table I was taken as $56\,160 - 380 = 55\,780\text{ cm}^{-1}$ for the emission calculations of the present section.

Table II shows a detailed comparison between the computed and observed positions and intensities of the zero-phonon lines. It includes, for the spectral domain of Fig. 2, all the transitions predicted to have an intensity larger than 0.5 times our arbitrary unit. Out of these 17 transitions, all the 6 π ones are indeed observed, along with 5 out of the 11 predicted σ ones (several other predicted σ transitions are seen in Fig. 2, but are not included in Table II because the associated experimental features could be due to noise as well). It is seen in Table II that the agreement between computed and observed zero-phonon lines is good, both for positions (columns b and d) and relative intensities (columns e and f). In particular, the $\Gamma_{5,6}$ symmetry of the lowest $4f^25d$ sublevel at $56\,160\text{ cm}^{-1}$ is fully supported by the polarization of all the observed zero-phonon lines. This sublevel corresponds to the lowest $4f^25d$ final state of the GSE spectrum measured at low temperature by Wegh, Donker and Meijerink,⁵ the location of which was found to be $56\,180 \pm 10\text{ cm}^{-1}$, and is in the margin of error of the lowest $4f^25d$ level estimated by Dorenbos at $56\,780 \pm 650\text{ cm}^{-1}$.¹⁶

To summarize this Section, the good agreement between theoretical and experimental emission spectra suggests that the emitting levels (the lowest ones of $4f^25d$) are well understood (symmetry and wave functions).

B. Ground- and excited-state absorption

Figure 3 shows the calculated and the experimentally measured $4f^3 \rightarrow 4f^25d$ GSA spectra as well as the experimentally measured GSE spectrum recorded by monitoring the $4f^25d \rightarrow 4f^3$ UV emission. The agreement between the curves corresponding to the two lower-energy bands centred at 175 and 155 nm is rather good, both qualitatively and quantitatively. The calculations, however, do not correctly reproduce the intensity and the position for the third band located around 140 nm. This is probably due to the crystal-field calculation method itself, which is not so reliable at the highest energies; admixture between $5d$ and other configuration states, indeed, is not taken into account, while it surely

TABLE II. Zero-phonon lines in emission at 12 K. Column (a): Terminal sublevel, with the same notations as in Table II of Ref. 12; Column (b): Expected position in cm^{-1} (*i.e.*, 56 160 minus terminal sublevel observed energy from Ref. 12); Column (c): Polarization; Column (d): Observed position in cm^{-1} (this work); Column (e): calculated intensity in arbitrary units (this work); and Column (f): Observed intensity (this work) multiplied by a suitable common normalization factor.

(a)	(b)	(c)	(d)	(e)	(f)	
${}^4F_{3/2}$	$\Gamma_{7,8a}$	44622	σ	44547	3.9	2.3
			π	44563	8.9	10.7
${}^4F_{3/2}$	$\Gamma_{5,6a}$	44559	σ		1.2	
${}^4F_{5/2}$	$\Gamma_{7,8a}$	43620	σ	43561	1.6	1.5
			π	43573	1.0	1.9
${}^4F_{5/2}$	$\Gamma_{5,6a}$	43609	σ		1.3	
${}^4F_{5/2}$	$\Gamma_{5,6b}$	43490	σ		0.6	
${}^4F_{7/2}$	$\Gamma_{5,6a}$	42635	σ		0.6	
${}^4F_{7/2}$	$\Gamma_{7,8b}$	42508	π	42445	0.8	0.5
${}^4G_{5/2}$	$\Gamma_{5,6a}$	38997	σ	38956	5.1	4.6
${}^4G_{5/2}$	$\Gamma_{7,8a}$	38887	σ	38865	6.6	6.5
			π	38885	1.6	1.5
${}^2G(1)_{7/2}$	$\Gamma_{5,6a}$	38747	σ		0.9	
${}^2G(1)_{7/2}$	$\Gamma_{7,8a}$	38739	π	38748	1.5	0.7
${}^2G(1)_{7/2}$	$\Gamma_{5,6b}$	38507	σ		1.0	
${}^4G_{7/2}$	$\Gamma_{7,8a}$	37089	π	37094	0.7	0.7
${}^4G_{7/2}$	$\Gamma_{5,6a}$	37079	σ	37051	0.8	1.6

exists. On the other hand, the discrepancy observed between the GSA and GSE experimental spectra is likely to be due to a decrease of fluorescence efficiency. Indeed, the forbidden band gap of LiYF_4 being equal to $85\,000\text{ cm}^{-1}$ (Ref. 17) and the ground state of Nd^{3+} ions in Nd:LiYF_4 being estimated at about $10\,000\text{ cm}^{-1}$ above the valence band,¹⁸ excitation in such high Nd^{3+} energy states should lead to photoionisation and trapping phenomena.

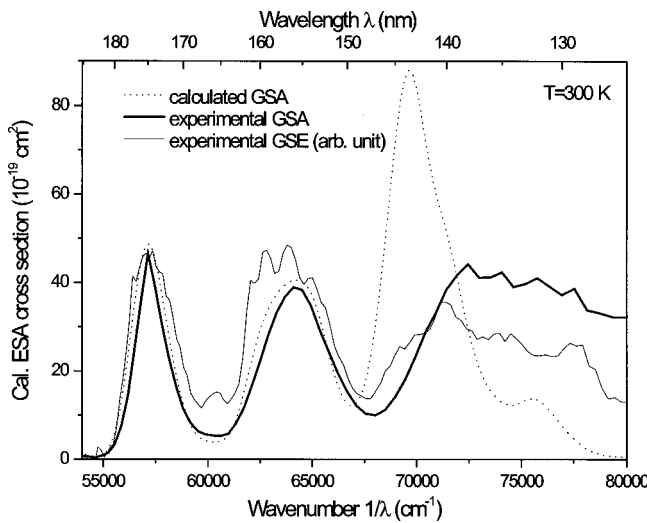


FIG. 3. Room-temperature unpolarized experimental and simulated ground-state absorption spectra and experimental ground-state excitation spectrum recorded by monitoring the 260-nm $4f^25d \leftrightarrow 4f^3$ emission. Vertical axis is in 10^{-19} cm^2 for the GSA spectra, in arbitrary units for the experimental GSE spectrum.

The calculated and experimental polarized ESA spectra from the ${}^4F_{3/2}$ level are presented in Figs. 4 and 5 at room and low temperatures, respectively. At room temperature, computed and experimental curves nicely agree in shape, but the measured cross sections are 1.5 times larger than the computed ones. The difference might arise from an improper choice of the $\langle r \rangle_{fd}$ parameter, but it could also be due to experimental uncertainties (difficulty to evaluate the pump energy absorbed by the sample, from which the number of $4f^3\text{ }{}^4F_{3/2}$ ions is deduced). The ESA cross sections are of the

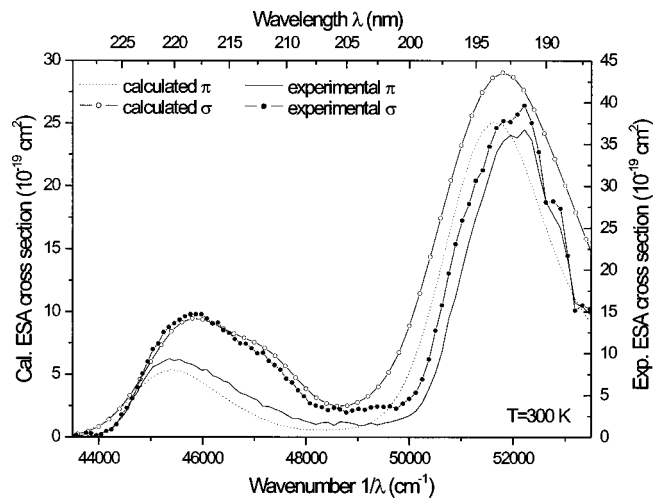


FIG. 4. Room-temperature polarized experimental and simulated excited-state absorption from ${}^4F_{3/2}$ level. Beware of different vertical scales, on the left for calculated cross sections and on the right for observed ones.

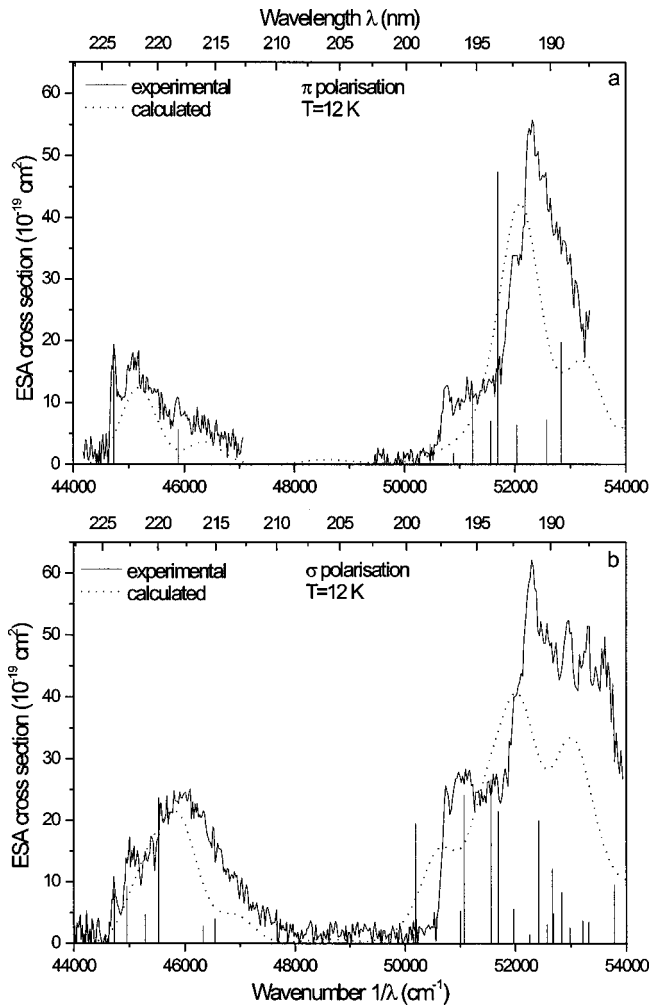


FIG. 5. Low-temperature experimental and simulated excited-state absorption from ${}^4F_{3/2}$ (a) in π and (b) in σ polarization. All curves are directly comparable to one another since no normalization factor has been introduced on the vertical axis. The vertical lines indicate the most intense predicted zero-phonon lines.

order of 10^{-18} cm^2 , which is characteristic of electric dipole allowed transitions. At room temperature, the maximum cross section for the first band is $1.5 \times 10^{-18} \text{ cm}^2$ at $45\,767 \text{ cm}^{-1}$ (218.5 nm) in σ polarization and $0.9 \times 10^{-18} \text{ cm}^2$ at $45\,558 \text{ cm}^{-1}$ (219.5 nm) in π polarization. In view of an up-conversion pumped vuv laser, this first ESA band is probably the most suitable one for the second excitation step by using, for example, the fifth harmonic (frequency-quintupled radiation) of a Nd-YAG laser at 213 nm.

As in the case of the emission spectra, the polarization character of the ESA bands from level ${}^4F_{3/2}$ is more pronounced at low temperature. Moreover, the 12 K spectra reported in Fig. 5 show at least four zero-phonon lines in π polarization ($44\,680$, $45\,880$, $50\,775$, $51\,960 \pm 50 \text{ cm}^{-1}$) and some others in σ , corresponding to transitions from the lowest ${}^4F_{3/2}$ Stark component to several states of the $4f^25d$ configuration. The real positions of these states can be obtained by adding to their observed positions the energy of the lowest ${}^4F_{3/2}$ sublevel ($11\,538 \text{ cm}^{-1}$ in Ref. 12). The first

zero-phonon line at $44\,680 \text{ cm}^{-1}$ thus represents a transition from the lowest ${}^4F_{3/2}$ sublevel to a final state located at $56\,220 \pm 50 \text{ cm}^{-1}$, which corresponds nicely to the lowest state of the $4f^25d$ configuration deduced from the emission spectra (Sec. IV A). The spectral separation between the position of the zero-phonon line and the maximum of the broadband, with a value of about $600 \pm 50 \text{ cm}^{-1}$, is greater than that in emission. Therefore, the parameter d'_0 was taken, for the absorption calculations, as $56\,160 + 600 = 56\,760 \text{ cm}^{-1}$. The difference between the d'_0 values for the absorption and emission spectra is due to the Stokes shift. The positions of the most intense theoretical zero-phonon lines are shown in Fig. 5. Only a few identifications could be done between calculated and observed zero-phonon lines, all of them being located in the low-energy part of the spectra (below $47\,000 \text{ cm}^{-1}$). For example, the π line at $45\,880 \text{ cm}^{-1}$ undoubtedly corresponds to the 6th sublevel of the $4f^25d$ configuration. On the other hand, the π lines observed at $50\,775$ and $51\,960 \text{ cm}^{-1}$ could not be reliably associated with calculated sublevels. The good agreement obtained with the ${}^4F_{3/2}$ ESA spectra below $47\,000 \text{ cm}^{-1}$ supports the conclusion of Sec. IV A; we understand reasonably well the detailed structure of the lowest part of the $4f^25d$ configuration. On the other hand, perhaps for lack of optimization of the Hamiltonian parameters, we obtain coarser results for higher energies. Currently, the numerous and closely packed $4f^25d$ sublevels which contribute to the right part in Figs. 4, 5(a), and 5(b) are not correctly described *individually* although their *global* effect is satisfactorily predicted.

After populating the ${}^4D_{3/2}$ level, the efficiency of the second step ${}^4D_{3/2} \rightarrow 4f^25d$ in the 230–350 nm range, which we had underestimated in a previous work,⁴ is now reassessed by our current ESA measurements (ESA cross sections around $5 \times 10^{-19} \text{ cm}^2$) and also confirmed theoretically (see Fig. 6). Moreover, the preliminary ESE spectrum published in Ref. 4 is now calibrated, thanks to ESA cross-section measurements in the 300–320 nm range, and it is also shown in Fig. 6. This ESE spectrum is in good agreement with the calculated lowest ${}^4D_{3/2} \rightarrow 4f^25d$ transition peak at 330 nm. Moreover, the calculated spectra of Fig. 6 confirm that the intensity of ESA from ${}^4D_{3/2}$ is twice stronger in σ polarization than in π polarization around 330 nm, as it was previously observed experimentally.⁴

In order to understand the reason for the weakness of ${}^4D_{3/2}$ ESA in the 230–350 nm domain, we compare in Fig. 7 the absorption spectra from ${}^4I_{9/2}$, ${}^4F_{3/2}$, and ${}^4D_{3/2}$ calculated at $T = 295 \text{ K}$ and for unpolarized light. We add respectively 0, 11 538, and $28\,110 \text{ cm}^{-1}$ to the abscissas, so that a given vertical line in Fig. 7 corresponds to the same energetic position within the $4f^25d$ configuration. Computed absorptions from ${}^4I_{9/2}$, ${}^4F_{3/2}$, and ${}^4D_{3/2}$ toward $4f^25d$ states have similar intensities, but the absorption maximum is shifted to higher $4f^25d$ energies when the considered initial $4f^3$ sublevel itself is at higher energies. Thus, level ${}^4D_{3/2}$ is not a “cursed” level; its low ESA cross section in the 230–350 nm wavelength domain merely arises from the fact that the strongest contribution to absorption is toward higher

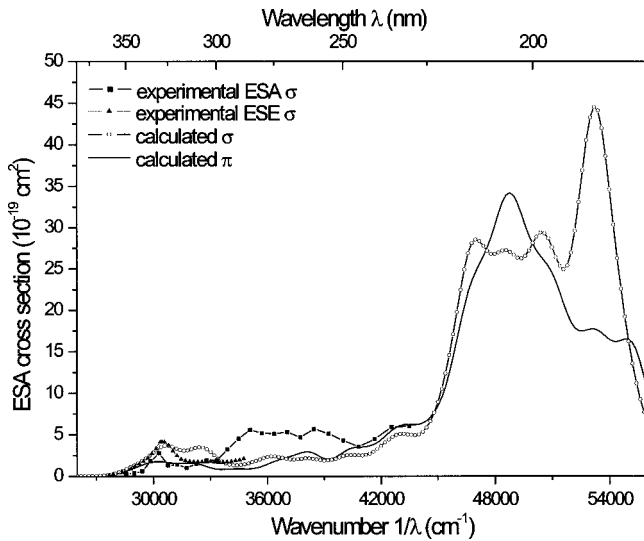


FIG. 6. Comparison between σ polarized experimental ${}^4D_{3/2}$ excited-state-excitation and -absorption spectra and polarized simulated ${}^4D_{3/2}$ excited-state absorption spectra at room temperature. The experimental ESA cross section at 330 nm in σ polarization is $(2.8 \pm 0.8) 10^{-19} \text{ cm}^2$.

$4f^25d$ sublevels, in a spectral region which our current experimental apparatus cannot reach.

In order to characterize the overall spectral position of the absorption spectrum from a given $4f^3$ sublevel or group of sublevels, we introduce its barycenter $\bar{\nu}$ as

$$\bar{\nu} = \frac{\int \nu \sigma(\nu) d\nu}{\int \sigma(\nu) d\nu}, \quad (4a)$$

where

$$\sigma(\nu) = [\sigma^0(\nu) + \sigma^+(\nu) + \sigma^-(\nu)]/3. \quad (4b)$$

In particular, if the calculation is performed at very low temperature, only one sublevel i' of the $4f^3$ configuration is

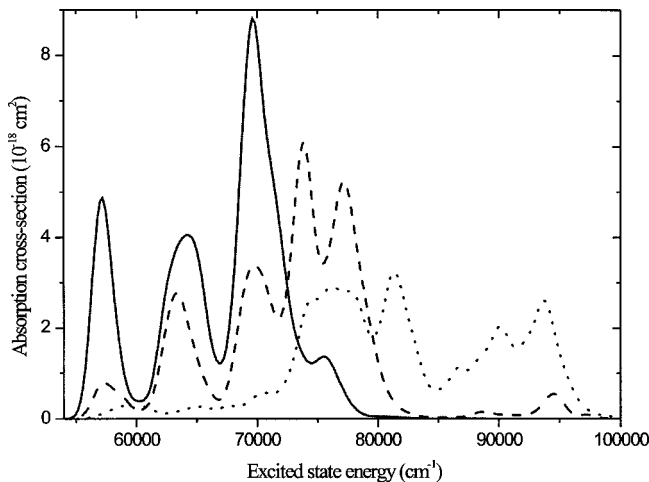


FIG. 7. Computed $4f^3 \rightarrow 4f^25d$ absorption spectra from ${}^4I_{9/2}$ (full line), ${}^4F_{3/2}$ (dashes), and ${}^4D_{3/2}$ (dots) for Nd^{3+} in LiYF_4 at 295 K, with unpolarized probe light.

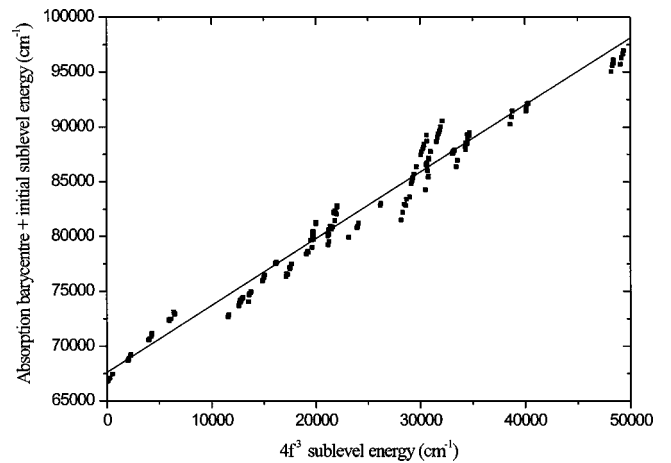


FIG. 8. Computed center of gravity ($\bar{\nu}_{i'} + E_{i'}$) of ESA at very low temperature as a function of the energy $E_{i'}$ of the initial $4f^3$ sublevel i' . The solid line is a least-square fit to the 175 computed points.

populated and we call $\bar{\nu}_{i'}$ the corresponding ESA (or GSA) barycenter.¹⁹ Let $E_{i'}$ be the eigenenergy of $4f^3$ sublevel i' . Figure 8 shows $(\bar{\nu}_{i'} + E_{i'})$ as a function of $E_{i'}$ for the 175 $4f^3$ sublevels that are energetically below the lowest $4f^25d$ sublevel. The plot clearly shows a positive slope; thus, the behavior observed in Fig. 7 for ${}^4I_{9/2}$, ${}^4F_{3/2}$, and ${}^4D_{3/2}$ remains valid for all $4f^3$ sublevels. The solid straight line in Fig. 8 is the least-squares fit to the points, its slope is 0.610. The points are obviously not randomly scattered around their least-squares line; for instance, one observes in the left-hand part of Fig. 8, below 7000 cm^{-1} , that the slope associated with the spin-orbit splitting of the 4I term is noticeably larger than the overall 0.610 and that, within a given 4I_J level, the slope associated with crystal-field effects is even bigger.

The qualitative physical explanation of Fig. 8 is obvious. Let us call (1), (2), and (3) the three $4f$ electrons in the initial $4f^3$ sublevel i' . When one of them, for instance (3), becomes $5d$ by absorption of a photon, electrons (1) and (2) are initially unaffected by the transition.²⁰ Therefore, the ion keeps some “memory” of its initial state i' when it undergoes a $4f^3 \rightarrow 4f^25d$ transition and the positive slope of Fig. 8 is a consequence of this memory. The chief contribution to the splitting of each of the two involved configurations arising from the electrostatic coupling H_{ee} ,²¹ it should be responsible for the 0.610 slope of Fig. 8. At first sight, one expects that one third of the average value $\langle \Psi_{i'} | H_{ee} | \Psi_{i'} \rangle$ should be preserved in the $4f^3 \rightarrow 4f^25d$ transition since the coupling between electrons (1) and (2) is unaltered during the optical transition, which is not the case for the couplings between electron (3) and each of the two other. Therefore, the slope of Fig. 8 should be 0.333. The fact that it is significantly larger suggests that the couplings (1)-(3) and (2)-(3) are not wholly randomized by the transition, but that they keep a partial memory of their previous values. The aim of the following section is to investigate this partial memory effect.

V. MOMENTUM CALCULATIONS

For absorption from a single $4f^3$ sublevel i' , Eq. (4a) may be rewritten as

$$\bar{\nu}_{i'} = \frac{\sum_{i,p} I_{i'i}^p \nu_{i'i}}{\sum_{i,p} I_{i'i}^p}, \quad (5)$$

where p runs over the three polarizations and i over all the $4f^2 5d$ sublevels.

Assuming that refraction index n does not depend on the wave number (an approximation already made to calculate Figs. 1 to 8), Eqs. (2) and (5) yield

$$\bar{\nu}_{i'} = \frac{\sum_{i,p} \nu_{i'i}^2 |\langle \Phi_i | D_p | \Psi_{i'} \rangle|^2}{\sum_{i,p} \nu_{i'i} |\langle \Phi_i | D_p | \Psi_{i'} \rangle|^2}. \quad (6)$$

In order to obtain simpler mathematical results, we drop one energy factor $\nu_{i'i}$ both in the numerator and the denominator of Eq. (6). It means that we replace the absorption cross section by the corresponding shape function;

$$f(\nu) = \frac{\sigma(\nu)}{\nu} \quad (7)$$

with barycenter

$$\bar{\nu}_{i'}^f = \frac{\sum_{i,p} \nu_{i'i} |\langle \Phi_i | D_p | \Psi_{i'} \rangle|^2}{\sum_{i,p} |\langle \Phi_i | D_p | \Psi_{i'} \rangle|^2}. \quad (8)$$

Writing $\nu_{i'i}$ in terms of expectation values of H in the i' and i states, we get

$$\begin{aligned} \bar{\nu}_{i'}^f + E_{i'} &\equiv \bar{\nu}_{i'}^f + \langle \Psi_{i'} | H | \Psi_{i'} \rangle \\ &= \frac{\sum_{i,p} \langle \Psi_{i'} | D_p^\dagger | \Phi_i \rangle \langle \Phi_i | H | \Phi_i \rangle \langle \Phi_i | D_p | \Psi_{i'} \rangle}{\sum_{i,p} |\langle \Phi_i | D_p | \Psi_{i'} \rangle|^2}. \end{aligned} \quad (9)$$

The denominator of Eq. (9) is readily evaluated as

$$\sum_{i,p} |\langle \Phi_i | D_p | \Psi_{i'} \rangle|^2 = \frac{9}{7} (\langle r \rangle_{fd})^2. \quad (10)$$

Thus, absorption has the same integrated intensity,²² whatever the initial sublevel i' , provided one considers the shape function [Eq. (7)] instead of the absorption cross section. We make now a further approximation. In Eq. (9) we replace the eigenstates $|\Psi_{i'}\rangle$ of H by the LS basis states $|f^3 \alpha SLJM\rangle$ which we shall call, for short, $|B_{j'}\rangle$. That means, we consider the following as approximate energy $E_{j'}^0$ of the f^3 sublevel j' :

$$E_{j'}^0 = \langle B_{j'} | H | B_{j'} \rangle, \quad (11)$$

and as barycenter of the $4f^2 5d$ states toward which j' absorbs:

$$\begin{aligned} \bar{\nu}_{j'}^f + E_{j'}^0 &= \frac{7}{9(\langle r \rangle_{fd})^2} \sum_{i,p} \langle B_{j'} | D_p^\dagger | \Phi_i \rangle \langle \Phi_i | H | \Phi_i \rangle \\ &\quad \times \langle \Phi_i | D_p | B_{j'} \rangle. \end{aligned} \quad (12)$$

The second member of Eq. (11) is a linear combination of ten Hamiltonian parameters only: $F^{(2)}(ff)$, $F^{(4)}(ff)$, $F^{(6)}(ff)$, α , β , γ , $\zeta(f)$, $B_{20}(f)$, $B_{40}(f)$, and $B_{60}(f)$, because operators $C_4^{(4)}$ and $C_4^{(6)}$ have no diagonal matrix elements on the $|B_{j'}\rangle$ basis. Let us write

$$E_{j'}^0 = \sum_{t=1}^{10} z_{j'}(t) \times P(t), \quad (13)$$

where $P(t)$, with $t=1, 2, \dots, 10$, is written for short, instead of $F^{(2)}(ff)$, $F^{(4)}(ff)$, \dots , $B_{60}(f)$.

Similarly, the second member of Eq. (12) is a linear combination

$$\bar{\nu}_{j'}^f + E_{j'}^0 = \sum_{t=1}^{18} y_{j'}(t) \times P(t), \quad (14)$$

where the first ten indices are the same as in Eq. (13) and the other eight label parameters that play no role in the $4f^3$ configuration hamiltonian matrix, namely, $t=11, 12, \dots, 18$ for $F^{(2)}(fd)$, $F^{(4)}(fd)$, $G^{(1)}(fd)$, $G^{(3)}(fd)$, $G^{(5)}(fd)$, $\zeta(d)$, $B_{20}(d)$, and $B_{40}(d)$ respectively [the $B_{44}(d)$ term in Eq. (12) vanishes].

Coefficients $z_{j'}(t)$ and $y_{j'}(t)$ defined by Eqs. (13) and (14) are not simple. But it can be demonstrated that with the exceptions of $y_{j'}(13)$, $y_{j'}(14)$, and $y_{j'}(15)$, each of the $y_{j'}(t)$ is proportional to some particular $z_{j'}(t')$, with a simple coefficient. The details of the calculations are omitted here, for the sake of brevity, and only the results are quoted. For $F^{(2)}(ff)$, $F^{(4)}(ff)$, $F^{(6)}(ff)$, α , β , and γ , one has merely

$$y_{j'}(t) = \frac{1}{3} z_{j'}(t), \quad (15)$$

in agreement with our intuitive result at the end of Sec. IV B: the operators associated with these six parameters are bielectronic; one pair of $4f$ electrons (out of three) is unaffected by the $4f \rightarrow 5d$ transition, therefore the average value of the Hamiltonian term is reduced by a factor of 3. Similarly, for $\zeta(f)$, $B_{20}(f)$, $B_{40}(f)$, and $B_{60}(f)$, one has $y_{j'}(t) = \frac{2}{3} z_{j'}(t)$: the operators associated with these four parameters are mono-electronic. Since two among the three $4f$ electrons are unaffected by the optical transition, the average value of the corresponding Hamiltonian term is multiplied by $2/3$.

The following relationships show to what extent the d electron keeps a partial memory of its previous state:

$$y_{j'}[F^{(2)}(fd)] = \frac{2}{3} \times \frac{6}{7} \times z_{j'}[F^{(2)}(ff)], \quad (16a)$$

$$y_{j'}[F^{(4)}(fd)] = \frac{2}{3} \times \frac{11}{21} \times z_{j'}[F^{(4)}(ff)], \quad (16b)$$

$$y_{j'}[\zeta(d)] = \frac{1}{3} \times \frac{2}{3} \times z_{j'}[\zeta(f)], \quad (16c)$$

$$y_{j'}[B_{20}(d)] = \frac{1}{3} \times \frac{6}{7} \times z_{j'}[B_{20}(f)], \quad (16d)$$

$$y_{j'}[B_{40}(d)] = \frac{1}{3} \times \frac{11}{21} \times z_{j'}[B_{40}(f)]. \quad (16e)$$

For bielectronic operators associated with parameters $F^{(k)}$ ($k=2$ or 4), factor $2/3$ arises from the fact that two out of the three electronic pairs are affected by the $4f \rightarrow 5d$ transition and factor

$$7 \begin{Bmatrix} 3 & k & 3 \\ 2 & 1 & 2 \end{Bmatrix} \frac{\langle d \| C^{(k)} \| d \rangle}{\langle f \| C^{(k)} \| f \rangle}$$

represents the loss of memory in the process (its numerical value is $6/7$ for $k=2$ and $11/21$ for $k=4$). Similarly, in the case of mono-electronic crystal-field operators associated with B_{20} and B_{40} , the first factor $1/3$ is associated with the fact that one electron is involved in the optical transition and the same factor as above ($6/7$ or $11/21$) accounts for the loss of memory. The spin-orbit operator is associated with the first factor $1/3$ (like other mono-electronic operators) and with a loss of memory factor

$$-7 \begin{Bmatrix} 3 & 1 & 3 \\ 2 & 1 & 2 \end{Bmatrix} \frac{\langle d \| I^{(1)} \| d \rangle}{\langle f \| I^{(1)} \| f \rangle},$$

which is equal to $2/3$.

The case of the exchange Coulomb parameters $G^{(1)}(fd)$, $G^{(3)}(fd)$, and $G^{(5)}(fd)$ is more complicated. One calculates for $t=13, 14$, or 15 , i.e., for $k=1, 3$, or 5

$$y_{j'}(t) = \sum_{\kappa=k-1}^{k+1} \frac{490}{3} (2\kappa+1) \times \begin{Bmatrix} 3 & 3 & \kappa \\ k & 1 & 2 \end{Bmatrix}^2 \begin{Bmatrix} 2 & k & 3 \\ 0 & 0 & 0 \end{Bmatrix}^2 \theta_{j'}(\kappa), \quad (17a)$$

$\theta_{j'}(\kappa)$ being defined as

$$\theta_{j'}(\kappa) \equiv \langle B_{j'} | u^{(\kappa)}_{(1)} \cdot u^{(\kappa)}_{(2)} + u^{(\kappa)}_{(2)} \cdot u^{(\kappa)}_{(3)} + u^{(\kappa)}_{(3)} \cdot u^{(\kappa)}_{(1)} | B_{j'} \rangle, \quad (17b)$$

where $u^{(\kappa)}_{(i)}$ are mono-electronic unit tensorial operators. For even values of κ , the second member of Eq. (17b) is proportional to $z_{j'}[F^{(\kappa)}(ff)]$. But for odd κ 's, $F^{(\kappa)}(ff)$ does not exist because $\begin{pmatrix} 3 & \kappa & 3 \\ 0 & 0 & 3 \end{pmatrix}$ is zero. Thus, according to Eq. (17a), $y_{j'}[G^{(k)}(fd)]$ is the sum of three terms, among which the first and the last ones are proportional to $z_{j'}[F^{(k-1)}(ff)]$ and $z_{j'}[F^{(k+1)}(ff)]$, respectively, but the second one is not related to any $z_{j'}(t')$. However, since all factors in Eq. (17a) are positive, exchange electrostatic terms too should contribute to the "partial memory" effect.

We come now to the interpretation of the slope of Fig. 8. We consider only the contributions of H_{ee} , the electrostatic part of the Hamiltonian. Let us write

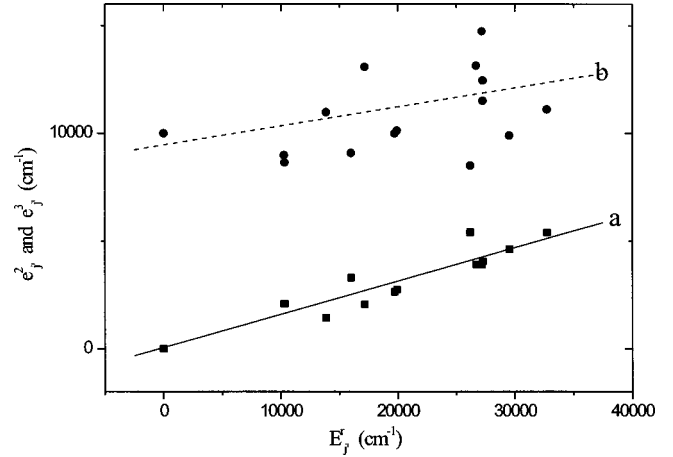


FIG. 9. Contributions to the approximate absorption barycenter ($e_{j'}^1 + e_{j'}^2 + e_{j'}^3$) from: (a) direct Coulomb $4f$ - $5d$ interaction $e_{j'}^2$, (squares, full least-squares line) and (b) exchange Coulomb $4f$ - $5d$ interaction $e_{j'}^3$, (circles, dashed least-squares line). For clarity, Fig. 9(b) has been displaced away from Fig. 9(a) by an arbitrary vertical amount.

$$E_{j'}^r = \sum_{t=1}^6 z_{j'}(t) \times P(t), \quad (18a)$$

$$e_{j'}^1 = \sum_{t=1}^6 y_{j'}(t) \times P(t), \quad (18b)$$

$$e_{j'}^2 = \sum_{t=11}^{12} y_{j'}(t) \times P(t), \quad (18c)$$

$$e_{j'}^3 = \sum_{t=13}^{15} y_{j'}(t) \times P(t). \quad (18d)$$

$E_{j'}^r$ corresponds, in the present approximation, to $E_{j'}^0$ of Eq. (13) and $e_{j'}^1 + e_{j'}^2 + e_{j'}^3$ to barycenter $\bar{v}_{j'}^{f0} + \bar{E}_{j'}^0$ of Eq. (14). $e_{j'}^1$, $e_{j'}^2$, and $e_{j'}^3$ are, respectively, the contributions arising from the Coulomb coupling of $4f$ electrons, from the direct Coulomb coupling of $4f$ and $5d$ electrons, and from the exchange coupling of $4f$ and $5d$ electrons.

From Eq. (15), one has exactly $e_{j'}^1 = \frac{1}{3} E_{j'}^r$, whatever the sublevel j' . On the other hand, from Eqs. (16a) and (16b),

$$e_{j'}^2 = \frac{4}{7} z_{j'}(1) F^{(2)}(fd) + \frac{22}{63} z_{j'}(2) F^{(4)}(fd), \quad (19)$$

which obviously does not have a one to one correspondence with $E_{j'}^r$ [Eq. (18a)]. Thus, in contradistinction with the case of $e_{j'}^1$, we cannot give a simple expression for the average slope of $e_{j'}^2$ versus $E_{j'}^r$. However, we can make a computer evaluation of the second member of Eq. (18c), using Eq. (12) for the calculation of the $y_{j'}(t)$'s and Table I for parameters $P(t)$.²³ Figure 9(a) shows $e_{j'}^2$ versus $E_{j'}^r$, together with the least-squares fit by a linear function, the slope of which is found to be 0.154 . This slope depends on the values we

assumed for the $F^{(k)}(ff)$ and the $F^{(k)}(fd)$. But it should not change much, provided these parameters keep physically reasonable values.

A fortiori, a one to one relationship is not expected between $e_{j'}^3$ and $E_{j'}^r$, since the former depends on several radial integrals which do not appear in the latter. Like in the case of the $e_{j'}^2$'s, we perform a numerical computation of the $e_{j'}^3$'s using Eq. (18d) and (12). Figure 9(b) shows the results; Although the points are much scattered, we observe a distinct tendency of $e_{j'}^3$ to increase with $E_{j'}^r$, and the slope of the least-squares fit is 0.088.

The predicted slope of Fig. 8 is, therefore, $0.333+0.154+0.088=0.575$, which is close to the ‘‘observed’’ value 0.610. The greatest part of the difference ($0.610-0.575=0.035$) arises from the substitution of the shape function to the absorption cross section; a computer simulation shows that it accounts for 0.027. Thus, we have been able to interpret physically more than 98.5% of the slope observed in Fig. 8 as due to the total or partial memory of the diagonal matrix elements of the electrostatic interaction H_{ee} during $4f^3 \rightarrow 4f^25d$ optical transitions.

VI. GENERAL CHARACTER OF THE MEMORY EFFECT AND CONSEQUENCES

The above results should be fairly general. First, since the origin of the memory effect is chiefly H_{ee} , the same consequences are expected, with only feeble differences, for the Nd^{3+} ion in any crystalline matrix; the center of gravity of the $4f^25d$ states reached by absorption should shift with energy $E_{i'}$ of the initial sublevel with a slope of the order of 0.6. Therefore, efficient absorption to the bottom of the $4f^25d$ configuration is not expected from high lying $4f^3$ levels in any neodymium-doped crystal.

Moreover, this memory effect should not be specific to Nd^{3+} . On the contrary, greater the number N of $4f$ electrons in the ground configuration, more complete the memory should be; factor $\frac{1}{3}$ of the present paper for $F^{(k)}(ff)$ terms becomes $((N-2)/N)$, which means that the center of gravity of the $4f^{N-1}5d$ states, reached by absorption, should follow

energy $E_{i'}$ of the initial sublevel even more closely for Er^{3+} or Tm^{3+} than for Nd^{3+} . We thus reach, for heavier rare-earth ions, even more pessimistic predictions concerning the possibility to efficiently populate the bottom of the $4f^{N-1}5d$ configuration through step by step pumping.

As an example, we understand now why one of us (M.L.) was unable, a few years ago, to observe ESA from $\text{Tm}^{3+}:\text{LiYF}_4$ 1G_4 , 1D_2 , and 1I_6 long-lived levels at 20 973, 27 961, and 34 729 cm^{-1} , respectively. With a probe beam in the 220–450 nm spectral range, it was hoped to reach the bottom of the $4f^{11}5d$ configuration from one of these levels. But a calculation similar to the one that leads to Figs. 3–7 shows that the $\text{Tm}^{3+} ^1G_4$ ESA cross section in this spectral domain should not be larger than $1.5 \times 10^{-20} \text{ cm}^2$ and those for 1D_2 and 1I_6 even smaller. In the case of 1D_2 , for instance, a 195-nm probe wavelength would have been necessary to obtain a cross section of $\sim 10^{-19} \text{ cm}^2$. Correlatively, the computed slope of the $(\bar{\nu}_{i'} + E_{i'})$ versus $E_{i'}$ plot (analogous to the present Fig. 8, but for the case of Tm^{3+}) is 0.918, out of which $10/12=0.833$ is accounted for by the total memory of the eleven $4f$ electrons that remain unaffected by the optical transition.

On the contrary, for Pr^{3+} , with $N=2$, there is no total memory of the electrostatic coupling, but only a partial one. The computed slope of the $(\bar{\nu}_{i'} + E_{i'})$ versus $E_{i'}$ plot amounts to 0.416 only, which results in more efficient populating of low $4f5d$ states through step by step pumping, as demonstrated, for instance, by the experimental results of Ref. 11.

ACKNOWLEDGMENTS

We are gratefully indebted to Dr. A. A. Tkatchuk (Laboratory of Spectroscopy of Crystals, S. I. Vavilov State Optical Institute, Saint Petersburg) for providing us with the Nd-doped LiYF_4 studied and to Dr. S. Girard for helpful discussion concerning the Tm^{3+} ESA experiments. This work was performed within the framework of the CNRS grant (Action coordonnée Optique) entitled ‘‘Cristaux dopés terres rares pour lasers UV accordables.’’

*Present address: CIRIL-ISMRA, 43 Blvd Maréchal Juin, 14050, Caen, France. FAX: 33 2 31 45 25 57.

¹R. W. Waynant and P. H. Klein, Appl. Phys. Lett. **46**, 14 (1985).

²M. A. Dubinskii, A. C. Cefalas, E. Sarantopoulou, S. M. Spyrou, C. A. Nicolaidis, R. Y. Abdulsabirov, S. L. Korableva, and V. V. Semashko, J. Opt. Soc. Am. B **9**, 1148 (1992).

³A. C. Cefalas, M. A. Dubinskii, E. Sarantopoulou, R. Abdulsabirov, S. T. Korableva, A. K. Naumov, V. V. Semashko, and C. A. Nicolaidis, Laser Chem. **13**, 143 (1993).

⁴Y. Guyot, S. Guy, and M.-F. Joubert, J. Alloys Compd. **323–324**, 722 (2001).

⁵R. T. Wegh, H. Donker, and A. Meijerink, Proc.-Electrochem. Soc. **97–99**, 284 (1988).

⁶M. A. Dubinskii, A. C. Cefalas, E. Sarantopoulou, R. Y. Abdulsabirov, S. L. Korableva, A. K. Naumov, and V. V. Semashko, Opt. Commun. **94**, 115 (1992).

⁷J. Thogersen, J. D. Gill, and H. K. Haugen, Opt. Commun. **132**, 83 (1996).

⁸P. W. Dooley, J. Thogersen, J. D. Gill, H. K. Haugen, and R. L. Brooks, Opt. Commun. **183**, 451 (2000).

⁹M. F. Reid, L. van Pieterse, R. T. Wegh, and A. Meijerink, Phys. Rev. B **62**, 14744 (2000).

¹⁰L. van Pieterse, M. F. Reid, R. T. Wegh, and A. Meijerink, J. Lumin. **94–95**, 79 (2001).

¹¹M. Laroche, J.-L. Doualan, S. Girard, J. Margerie, and R. Moncorgé, J. Opt. Soc. Am. B **17**, 1291 (2000).

¹²H. De Leebeek and C. Görller-Walrand, J. Alloys Compd. **225**, 75 (1995).

¹³J. Sugar, J. Opt. Soc. Am. **55**, 1058 (1965).

¹⁴J. Sugar and V. Kaufman, J. Opt. Soc. Am. **62**, 562 (1972).

¹⁵C. A. Morrison and R. P. Leavitt, J. Chem. Phys. **71**, 2366 (1979).

¹⁶P. Dorenbos, J. Lumin. **91**, 155 (2000).

- ¹⁷J. C. Krupa and M. Queffelec, *J. Alloys Compd.* **250**, 287 (1997).
- ¹⁸O. Guillot-Noël, B. Bellamy, B. Viana, and D. Gourier, *Phys. Rev. B* **60**, 1668 (1999).
- ¹⁹Most $4f^3$ sublevels i' have too short a lifetime to allow measurement of the corresponding ESA and therefore experimental determination of their $\bar{\nu}_{i'}$.
- ²⁰Shortly afterwards, the wave functions of electrons (1) and (2) are modified by coupling with the $5d$ electron in order to yield the final eigenfunction $|4f^25d, \Phi_i\rangle$, but this recoupling does not modify significantly the barycentre of the absorption spectrum.
- ²¹According to Ref. 11, this is not the case for Pr^{3+} , but it is true for Nd^{3+} , and even more so if the number of $4f$ electrons increases further from 4 to 7 ($\text{Pm}^{3+}, \dots, \text{Gd}^{3+}$).
- ²²This conclusion should probably be reconsidered if we choose a more realistic model where $4f^25d$ would no longer be isolated from higher configurations and conduction band states.
- ²³More precisely, since the current approximation only deals with the chief term H_{ee} of the Hamiltonian, we evaluate $e_{j'}^2$ for each of the 15 terms of $4f^3$ which lie below the lowest sublevel of $4f^25d$ configuration. For the least-squares fit of Fig. 9, each of the 15 points is taken with a weight $(2S+1)(2L+1)$.